

Electronic structures and topological properties of $TeSe_2$ monolayers

Zhengyang Wan(万正阳), Hao Huan(郇昊), Hairui Bao(鲍海瑞), Xiaojuan Liu(刘晓娟), and Zhongqin Yang(杨中芹)

Citation: Chin. Phys. B, 2021, 30 (**11**): 117304. DOI: 10.1088/1674-1056/ac2489
Journal homepage: http://cpb.iphy.ac.cn; http://iopscience.iop.org/cpb

What follows is a list of articles you may be interested in

Two-dimensional topological semimetals

Xiaolong Feng(冯晓龙), Jiaojiao Zhu(朱娇娇), Weikang Wu(吴维康), and Shengyuan A. Yang(杨声远)
Chin. Phys. B, 2021, 30 (**10**): 107304. DOI: 10.1088/1674-1056/ac1f0c

Progress on 2D topological insulators and potential applications in electronic devices

Yanhui Hou(侯延辉), Teng Zhang(张腾), Jiatao Sun(孙家涛), Liwei Liu(刘立巍), Yugui Yao(姚裕贵), Yeliang Wang(王业亮)
Chin. Phys. B, 2020, 29 (**9**): 097304. DOI: 10.1088/1674-1056/aba9c5

Improvement of valley splitting and valley injection efficiency for graphene/ferromagnet heterostructure

Longxiang Xu(徐龙翔), Wengang Lu(吕文刚), Chen Hu(胡晨), Qixun Guo(郭奇勋), Shuai Shang(尚帅), Xiulan Xu(徐秀兰), Guanghua Yu(于广华), Yu Yan(岩雨), Lihua Wang(王立华), Jiao Teng(滕蛟)
Chin. Phys. B, 2020, 29 (**7**): 077304. DOI: 10.1088/1674-1056/ab8db2

Topology and ferroelectricity in group-V monolayers

Mutee Ur Rehman, Chenqiang Hua(华陈强), Yunhao Lu(陆赟豪)
Chin. Phys. B, 2020, 29 (**5**): 057304. DOI: 10.1088/1674-1056/ab81ff

Recent progress on the prediction of two-dimensional materials using CALYPSO

Cheng Tang(唐程), Gurpreet Kour, Aijun Du(杜爱军)
Chin. Phys. B, 2019, 28 (**10**): 107306. DOI: 10.1088/1674-1056/ab41ea

---

Electronic structures and topological properties of $TeSe_2$ monolayers*

Zhengyang Wan(万正阳)[1], Hao Huan(郇昊)[1], Hairui Bao(鲍海瑞)[1], Xiaojuan Liu(刘晓娟)[1], and Zhongqin Yang(杨中芹)[1,2,†]

[1] *State Key Laboratory of Surface Physics and Key Laboratory of Computational Physical Sciences (MOE) & Department of Physics, Fudan University, Shanghai* 200433, *China*

[2] *Collaborative Innovation Center of Advanced Microstructures, Nanjing* 210093, *China*

(Received 27 July 2021; revised manuscript received 2 September 2021; accepted manuscript online 8 September 2021)

The successfully experimental fabrication of two-dimensional Te monolayer films [*Phys. Rev. Lett.* **119** 106101 (2017)] has promoted the researches on the group-VI monolayer materials. In this work, the electronic structures and topological properties of a group-VI binary compound of $TeSe_2$ monolayers are studied based on the density functional theory and Wannier function method. Three types of structures, namely, α-$TeSe_2$, β-$TeSe_2$, and γ-$TeSe_2$, are proposed for the $TeSe_2$ monolayer among which the α-$TeSe_2$ is found being the most stable. All the three structures are semiconductors with indirect band gaps. Very interestingly, the γ-$TeSe_2$ monolayer becomes a quantum spin Hall (QSH) insulator with a global nontrivial energy gap of 0.14 eV when a 3.5% compressive strain is applied. The opening of the global band gap is understood by the competition between the decrease of the local band dispersion and the weakening of the interactions between the Se p_x, p_y orbitals and Te p_x, p_y orbitals during the process. Our work realizes topological states in the group-VI monolayers and promotes the potential applications of the materials in spintronics and quantum computations.

Keywords: two-dimensional material, monolayer $TeSe_2$, quantum spin Hall effect, topological insulator

PACS: 73.22.–f, 73.43.Nq, 31.15.es, 31.15.ae **DOI:** 10.1088/1674-1056/ac2489

1. Introduction

Since the discovery and successful fabrication of graphene,[1] two-dimensional (2D) materials have attached intensive attention because of their many novel physical properties, such as the quantum spin Hall (QSH) effect,[2] quantum anomalous Hall (QAH) effect,[3] valley Hall effect,[4] etc, making them be promising candidate materials for future high performance electronic, spintronic, and optoelectronic devices.[4–7] Currently, besides graphene,[8,9] various types of 2D materials have also been synthesized in experiments, including elemental 2D films from group III to group V, such as boronene,[10–12] silicene,[13–15] stanine,[16] black phosphorus films,[17–19] antimonene,[20,21] and bismuthine.[22] Some binary 2D compounds such as MoS_2[23–26] and CrI_3[27] and so on were also fabricated successfully. Although plenty of 2D materials were reported owning QSH or QAH effects,[2,28,29] only few systems having the QSH (such as the HgTe/CdTe[30] quantum well and bismuthine[22]) or QAH (such as Cr doped $(Bi,Sb)_2Te_3$ film[31]) effects were confirmed in experiments.

Based on previous developments, researchers have extended the 2D materials to group-VI monolayers. In 2017, Zhu *et al.*[32] studied the structures and stability of tellurene (2D Te monolayers) using the particle-swarm optimization method in combination with density functional theory. And bilayer tellurene films have been observed in their experiments.[32] Different from two atomic layers in silicene and black phosphorus monolayers, tellurene contains trilayers,[32] with the central-layer Te behaving metal-like and the two outer layers semiconductor-like. They found that this unique multivalent behavior of Te guarantees the structural stability of the material.[32] Yan *et al.* found two ultra-stable novel allotropes for Te few-layers from first-principles calculations.[33] These studies promoted the researches on the group-VI monolayer materials. It is meaningful to explore the electronic structures and the interesting topological effects in group-VI monolayer materials.

In this work, the electronic structures and topological properties of a group-VI binary compound of $TeSe_2$ monolayers are studied based on the density functional theory and Wannier function method. Three types of structures, namely, α-$TeSe_2$, β-$TeSe_2$, and γ-$TeSe_2$, are proposed and studied, all of which are semiconductors with indirect band gaps. The γ-$TeSe_2$ monolayer is found being a QSH insulator with a global nontrivial energy gap of 0.14 eV when a 3.5% compressive strain is applied. The topology of the material is identified by the calculations of Z_2 topological invariants and the edge state. The opening mechanism of the global nontrivial band gap is analyzed.

2. Computational models and methods

For the 2D trilayered tellurene, the multiple valences of Te atoms promote the formation of a stable monolayer

*Project supported by the National Natural Science Foundation of China (Grant Nos. 11574051 and 11874117) and Natural Science Foundation of Shanghai, China (Grant No. 21ZR1408200).

†Corresponding author. E-mail: zyang@fudan.edu.cn

© 2021 Chinese Physical Society and IOP Publishing Ltd

tellurene structure. Based on the studied structures of tellurene[32] and tellurium few-layers,[33] we build and consider three typical structures for the $TeSe_2$ monolayers. To obtain the $TeSe_2$, the Te atoms in the two outer layers of tellurene are all replaced by Se atoms. Since Se electronegativity is larger than that of Te, the $TeSe_2$ structures are expected to be also very stable. The built three type structures for the $TeSe_2$ monolayers, named α, β, and γ phases, are illustrated in Figs. 1(a)–1(c), respectively. The α-$TeSe_2$ has a similar structure to that of 1T-MoS_2.[34] Both the Se1 and Se2, corresponding to the S atoms in the 1T-MoS_2, are in the outer layers of the materials, with the coordination number of 3. The central-layer Te atoms correspond to the Mo atoms in the 1T-MoS_2, with the coordination number of 6. For the β-$TeSe_2$, it presents a corrugated structure. In the top view, the structure is composed of hexagons and rhombuses. The coordination number of each Te atom in the β-$TeSe_2$ is 4, different from that in the α-$TeSe_2$. The γ-$TeSe_2$ has a similar geometric structure to that of 2H-MoS_2,[34] with an in-plane mirror symmetry. Exotic properties may be dug out from these various structures of the $TeSe_2$ monolayers.

The electronic states of the $TeSe_2$ monolayers with the three type structures are calculated within the framework of density functional theory (DFT), as implemented in the Vienna *ab initio* simulation package (VASP).[35] The projected augmented wave (PAW) potentials are adopted to deal with the electron–ion interactions.[36,37] The Perdew–Burke–Ernzerhof generalized gradient approximation (GGA-PBE) is used for the exchange–correlation functional.[38] A vacuum layer of 20 Å is applied between the neighboring $TeSe_2$ layers to minimize the image interactions from the periodic boundary condition. The plane wave cutoff energy is set to be 500 eV. The Γ-centered k-point sampling of $15 \times 15 \times 1$ is adopted in the first Brillouin zone. The structures are optimized until the force on each atom is less than 0.01 eV/Å. To investigate the dynamic stability of the proposed $TeSe_2$ ML, phonon dispersion is calculated by using the DFT perturbation theory as implemented in the PHONOPY code. The Z_2 topological invariant is calculated with the maximally localized Wannier functions[39] by using the Wannier 90 package. To obtain the edge states, we construct a TB Hamiltonian with a basis of maximally localized Wannier functions by using the Wannier Tools[40] package.

3. Results and discussion

3.1. Structures and electronic states of the $TeSe_2$ monolayers

We now study the geometric structures and the electronic states of the $TeSe_2$ monolayers with the three type structures (Figs. 1(a)–1(c)). The optimized structural parameters and the calculated cohesive energies of the three materials are listed in Table 1. The bond lengths of the neighboring Te and Se atoms (2.82–2.87 Å) are close to each other for the three structures studied. Due to the largest area of the 2D unit cell in β-$TeSe_2$, the layer thickness (d_z) in β-$TeSe_2$ is the smallest, corresponding to the smallest angle (θ) between the Te–Se bond and the horizontal direction (Table 1). In γ-$TeSe_2$, the Se1 is exactly localized on the top of the Se2. The strong repulsive forces between the two type anions (Se1 and Se2) result in the largest layer thickness in the structure, as seen from Table 1. Among the three structures, α-$TeSe_2$ has the largest cohesive energy while γ-$TeSe_2$ has the smallest one. Thus, α-$TeSe_2$ is the most stable structure and the other two structures are metastable. The first Brillouin zones of α-$TeSe_2$ (γ-$TeSe_2$) and β-$TeSe_2$ are hexagon and rectangle, respectively (Fig. 1(d)).

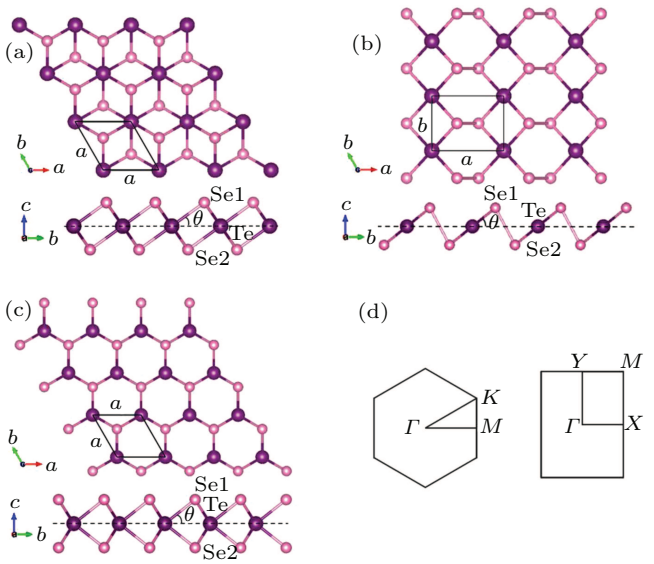


Fig. 1. Top and side views of the optimized structures of α-$TeSe_2$ (a), β-$TeSe_2$ (b), and γ-$TeSe_2$ (c). (d) The first Brillouin zones of α-$TeSe_2$ or γ-$TeSe_2$ (left) and β-$TeSe_2$ (right).

The calculated band structures of α-$TeSe_2$, β-$TeSe_2$, and γ-$TeSe_2$ are displayed in Figs. 2(a)–2(c), respectively. The Fermi level (E_F) is set at energy zero. The red dotted and the black solid curves present the bands for the materials without and with spin–orbit coupling (SOC) interactions, respectively. The SOC interactions do not change much the bands on the whole but can split the energy degeneracy at some positions in the momentum space, such as the places marked by the green ovals in Figs. 2(a) and 2(c). The three materials are all semiconductors with indirect band gaps. The SOC interactions slightly reduce the band gaps due to the energy splitting. The energy bands of α-$TeSe_2$ and β-$TeSe_2$ with SOC are both doubly degenerate, while the bands of γ-$TeSe_2$ are not. The reason is that both time-reversal and space-inversion symmetries are owned by the α-$TeSe_2$ and β-$TeSe_2$ monolayers, while there is no space-inversion symmetry in the γ-$TeSe_2$ monolayer (Fig. 1). In Figs. 2(a)–2(c), three group bands are clearly observed in the band structures of α-$TeSe_2$ and γ-$TeSe_2$. This similarity can be ascribed to the relatively similar structures of the two materials (Figs. 1(a) and 1(c)).

Table 1. The results for the monolayer $TeSe_2$ with different structures. The properties listed contain the lattice constants a and b, distance between the upper and lower Se atomic layers (d_z), Te–Se bond length, angle between the Te–Se bonding direction and the horizontal direction (θ, marked in Fig. 1), and the cohesive energy (E_c).

Type	Lattice parameters (Å)	d_z (Å)	Bond length (Å)	θ (°)	E_c (eV/atom)
			Te–Se		
α-$TeSe_2$	$a = b = 3.98$	3.32	2.83	35.85	2.86
β-$TeSe_2$	$a = 5.24$, $b = 3.67$	2.79	2.82	29.83	2.79
γ-$TeSe_2$	$a = b = 3.84$	3.65	2.87	39.48	2.71

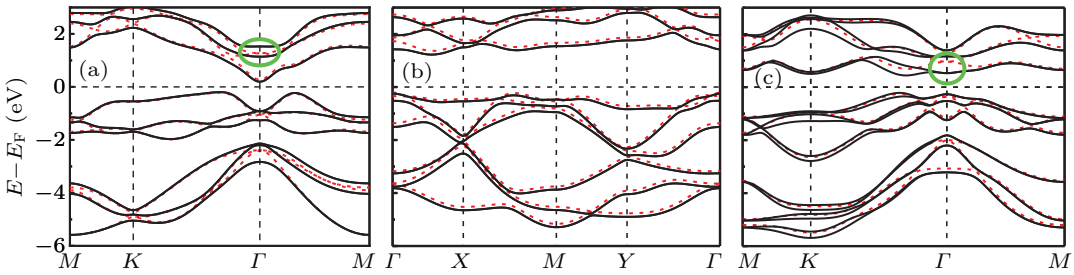


Fig. 2. Band structures of α-$TeSe_2$ (a), β-$TeSe_2$ (b), and γ-$TeSe_2$ (c) without (red dotted curves) and with (black solid curves) the consideration of SOC.

The similar structures of α-$TeSe_2$ and γ-$TeSe_2$ also give rise to the close band gaps of the two materials (Fig. 3(a)). When the SOC is turned on, the band gaps of α-$TeSe_2$ and γ-$TeSe_2$ are 0.38 eV and 0.65 eV, respectively. The obtained energy bands of β-$TeSe_2$ are given in Fig. 2(b), which are consistent with the results reported in Ref. [41]. The largest band gaps achieved in β-$TeSe_2$ (Fig. 3(a)) can be ascribed to the relatively flat bands localized at the valence-band top and conduction-band bottom in the material (Fig. 2(b)). The analysis of the orbital-resolved bands (not shown) shows that these flat bands are primarily composed of the p_z orbitals of the Se1 and Se2 atoms. Thus, the dangling bonds of the Se p_z orbitals in the unique β-$TeSe_2$ structure cause the relatively large band gaps in the materials.

For α-$TeSe_2$ (γ-$TeSe_2$), before the SOC is taken into account, doubly degenerate bands around 1.3 eV (1.0 eV) marked by green ovals occur, composed mainly by p_x and p_y orbitals of the Te and Se atoms (to be discussed), due to the C_{3v} symmetry in the monolayers. This degeneracy is lifted after the SOC is turned on. A pretty large direct band gap of 0.4/0.7 eV is opened there by the SOC in the α-$TeSe_2$/γ-$TeSe_2$ monolayer due to the stronger intrinsic SOC coming from the p_x and p_y orbitals, compared to that from the p_z orbitals.[42,43] The gaps opened in such kind of parabolic bands are generally topologically nontrivial, leading to the appearing of the QSH[44] or QAH[45,46] insulators with a non-Dirac-type band-gap opening mechanism. Since the concerned band gaps in $\alpha$$TeSe_2$ and γ-$TeSe_2$ are nonglobal, the materials are in topological semimetal states. As displayed in Fig. 2(a), the dispersion of the bands around 1.3 eV of α-$TeSe_2$ is very large. Expectably, it is difficult to tune the bands to produce a global topologically nontrivial band gap in the α-$TeSe_2$ monolayer. Therefore, the γ-$TeSe_2$ monolayer is focused in the following.

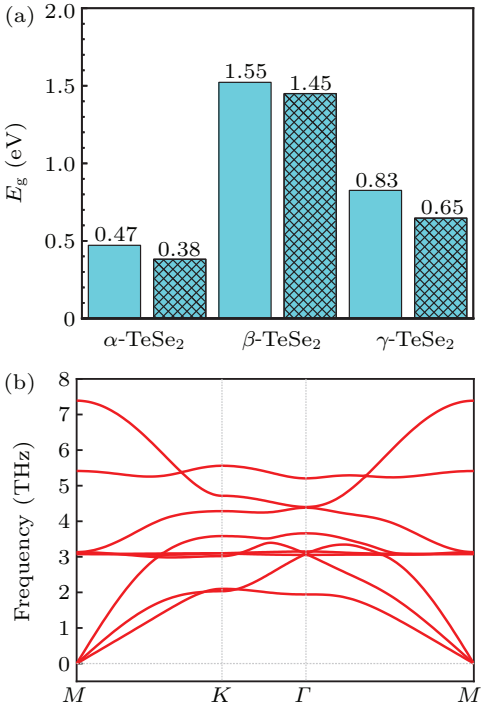


Fig. 3. (a) The band gaps of the three materials studied. The rectangles without and with the grids give the band gaps without and with the consideration of SOC. (b) The phonon spectrum of the γ-$TeSe_2$ monolayer.

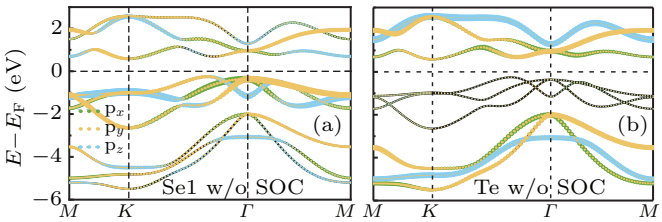


Fig. 4. The energy band projection of the Se1 (a) and Te (b) atoms in the γ-$TeSe_2$ monolayer without the consideration of SOC. The green, yellow, and blue colors represent the contributions from the p_x, p_y, and p_z orbitals of the corresponding atom, respectively.

In terms of the stability of the γ-$TeSe_2$ structure, the phonon spectrum is calculated and shown in Fig. 3(b). No

negative frequency is found in Fig. 3(b), indicating the dynamic stability of the γ-$TeSe_2$ despite its lowest cohesive energy among the three structures. To deeply understand the electronic structure of γ-$TeSe_2$, the projected band structures of the Se1 and Te atoms are plotted in Fig. 4 without considering SOC. Due to the in-plane mirror symmetry owned by γ-$TeSe_2$ (with D_{3h} space group), the upper layer Se1 and the lower layer Se2 atoms are equivalent. Therefore, only the band projection of the Se1 atom is analyzed. As shown in Figs. 4(a) and 4(b), the valence-band top and conduction-band bottom at the Γ point, with double degeneracy, are mainly contributed by the p_x and p_y orbitals of the Te or Se atoms. The degeneracy is lifted after the SOC is turned on. From the orbital distribution of the Se1 and Te atoms (Fig. 4), we can clearly find the bonding, nonbonding, and antibonding characteristics between the Se and Te atoms. The bonding states are formed between -6 eV and -2 eV. The nonbonding states are formed between -2 eV and 0 eV and antibonding states are formed between 0.5 eV and 2.8 eV.

3.2. Strain effects in γ-$TeSe_2$

As an effective means to tune electronic structures, strain has been applied in multiple material systems.[47–50] We here apply in-plane biaxial strain to the γ-$TeSe_2$ monolayer, which is defined as $\varepsilon = (a - a_0)/a_0$, where a (a_0) is the strained (unstrained) in-plane lattice constant. The positive and negative values of ε correspond to the tensile and compressive biaxial strains, respectively. The band evolution of γ-$TeSe_2$ under different biaxial strain is shown in Fig. 5. The bands we concern are located near 1.0 eV above the E_F around the Γ point, indicated by a yellow rectangle in Fig. 5(d).

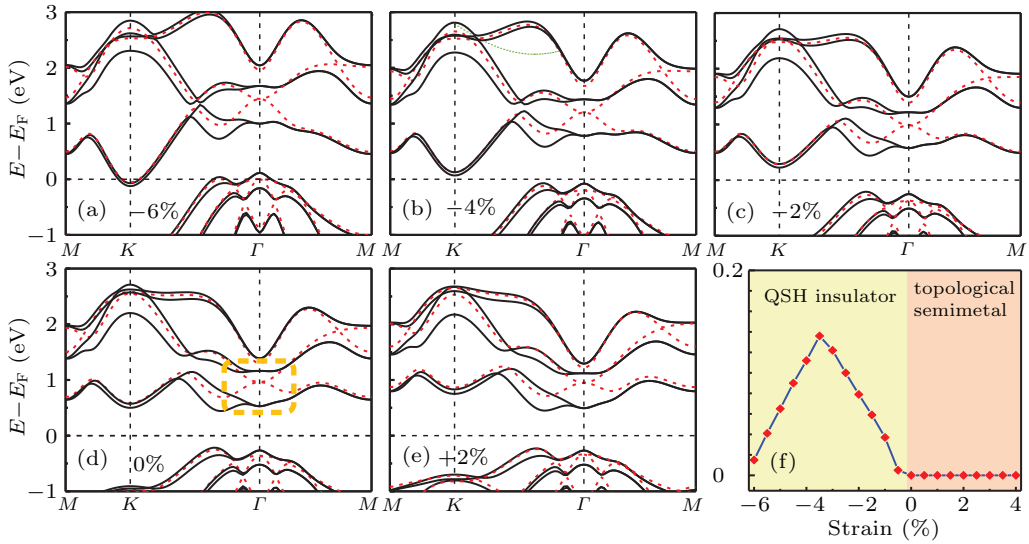


Fig. 5. (a)–(e) The band structures of the γ-$TeSe_2$ monolayer under strain of different strengths. The red dotted and black solid curves give the bands without and with SOC, respectively. (f) The global band gap as a function of the strain for the γ-$TeSe_2$ monolayer. Obvious topological phase transition occurs with compressive strain applied.

As shown in Fig. 5, with the increase of the compressive strain (from Fig. 5(d) to Fig. 5(a)), the relative position of the characteristic doubly degenerate bands at the Γ point moves to high energy region (from 1.0 eV in Fig. 5(d) to 1.4 eV in Fig. 5(a)). Clearly, the dispersion of the local bands along the K–Γ path in this energy region decreases in the process, which is beneficial to the opening of the global band gap. In the same process, the minimum band gap along the K–Γ path, however, decreases, hampering the opening of the global band gap. The competition of these two respects gives rise to the global band gap increasing first and then decreasing as the increase of the compressive strain, as displayed in Fig. 5(f). The global band gap of the system reaches the maximum of 0.14 eV with the strain of $\varepsilon = -3.5\%$. In the absence of strain or under tensile strain, the γ-$TeSe_2$ monolayer owns a semimetallic state with a higher electronic conduction performance than the semiconductors because of its 'quasi' metallic band structures.

The movement of the doubly degenerate bands at the Γ point (marked by the yellow rectangle in Fig. 5(d)) under the compressive strain can be comprehended by the orbital-resolved densities of states (DOSs) of the Se1 and Te atoms shown in Fig. 6. Note that due to the C_{3v} symmetry owned by the γ-$TeSe_2$ monolayer, the DOSs of p_x and p_y orbitals of the Se1 (also Te) atoms are completely overlapped in Fig. 6. The unoccupied states of the Te atom are much more than that of the Se atoms, hinting the charge transfer from the Te to Se atoms, consistent with the above analysis. These multivalent states, similar to the cases of the tellurene and MoS_2 systems, ensure the structural stability of the γ-$TeSe_2$ monolayer. In Fig. 6(a), the Se1 p orbitals are mainly distributed between -2 eV and -0.5 eV together with a few distributions between -6 eV and -2 eV or between 0.5 eV and 2.8 eV. The Te p orbitals are mainly distributed between -6 eV and -2 eV or between 0.5 eV and 2.8 eV. Unlike the Se1 atom, the Te p orbitals are not distributed between -2 eV and -0.5 eV, corresponding to the nonbonding state between Te and Se as discussed

in Fig. 4. With the increase of the compressive strain, the Te–Se bond length decreases (Table 2). Thus, the Te–Se bonds become strong, leading to the bonding and antibonding states moving to the lower and higher energy regions, respectively. This trend can be seen obviously from Figs. 6(a)–6(d). For example, the antibonding states of the Te and Se atoms move from the energy region of 0.5–1.5 eV in Fig. 6(a) to the energy region of 0.8–3.0 eV in Fig. 6(c). This behavior rationalizes well the movement to a high energy of the doubly degenerate bands at the Γ point marked in Fig. 5(d) with the increase of the compressive strain.

Table 2. The structural parameters of the γ-$TeSe_2$ monolayer under strain, including the layer thickness d_z in the z direction, bond lengths of Te–Se and Te–Te, and angle θ between the Te–Se bonding direction and the horizontal direction (shown in Fig. 1).

Strain (%)	d_z (Å)	Bond length (Å)		θ (°)
		Te–Se	Te–Te	
+2	3.61	2.89	3.92	38.57
0	3.65	2.87	3.84	39.48
–2	3.70	2.85	3.76	40.42
–4	3.75	2.84	3.69	41.39
–6	3.81	2.81	3.61	42.44

We now understand the variation of the local band gap, marked by the red circle in Fig. 7(a), for γ-$TeSe_2$ under the compressive strain. As displayed in Fig. 7, this local band gap is opened due to the direct interactions between the p_x, p_y (also few p_z) orbitals of Se and the p_x, p_y orbitals of Te. With the increase of the compressive strain, the band gap decreases. The reason can be due to the decrease of the interactions between the p_x, p_y orbitals of Se and the p_x, p_y orbitals of Te. With the increase of the compressive strain, the layer thickness (d_z) increases (Table 2), causing the increase of the distance between Se and Te along the z direction. Thus, the direct interactions between the p_x, p_y orbitals of Se and the p_x, p_y orbitals of Te decrease. This trend is not beneficial for opening the global band gap after the SOC is taken into consideration. The combination of the variation of the band gap (marked by the red circle in Fig. 7(a)) and the movement to a high energy of the doubly degenerate bands (marked by the red triangle in Fig. 7(a)) under strain produces the global band gap increasing first and then decreasing with the increase of the compressive strain, as shown in Fig. 5(f). The movement to a high energy of the doubly degenerate bands around 1.0 eV in Fig. 7(a) with the increase of the strain reflects the dispersion decrease of the local bands along the K–Γ path in the process. Thus, the opening of the global band gap in the γ-$TeSe_2$ monolayer can be understood by the competition between the decrease of the local band dispersion and the weakening of the interactions between the Se p_x, p_y orbitals and Te p_x, p_y orbitals during the process.

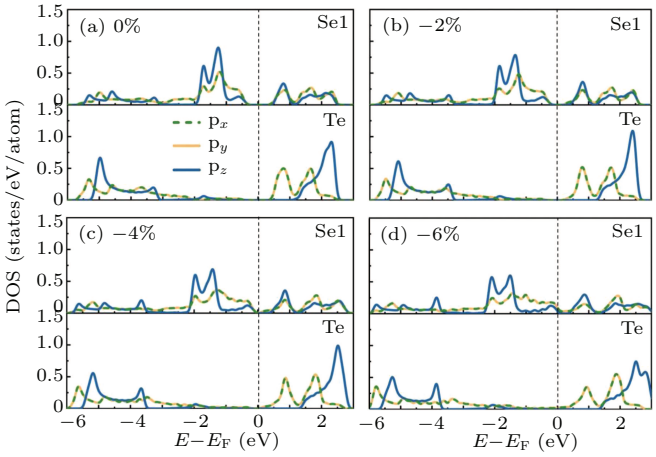


Fig. 6. (a)–(d) The orbital-resolved densities of states of Se1 and Te atom in the γ-$TeSe_2$ monolayer without and with −2%, −4%, and −6% strain, respectively. The SOC is not considered. The green, yellow, and blue colors represent the contributions from the p_x, p_y, and p_z orbitals of the corresponding atom, respectively.

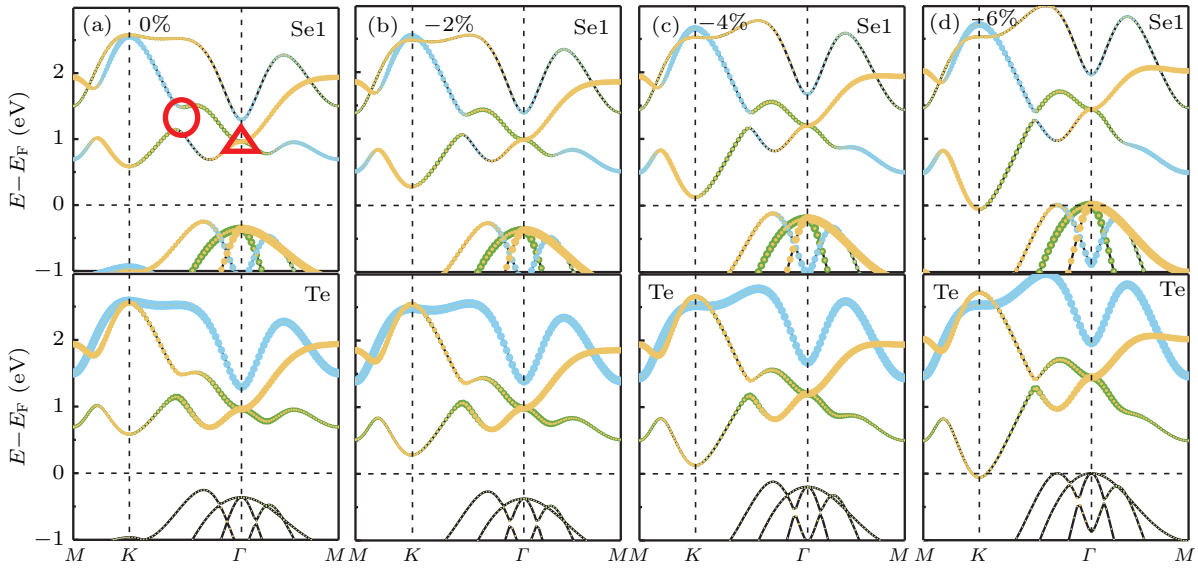


Fig. 7. (a)–(d) The energy band projection of the Se1 and Te atoms in the γ-$TeSe_2$ monolayer without and with −2%, −4%, and −6% strain, respectively. The SOC is not considered. The green, yellow, and blue colors represent the contributions from the p_x, p_y, and p_z orbitals of the corresponding atom, respectively.

3.3. Topological properties of γ-$TeSe_2$

Since the concerned global band gap is located around 1.2 eV above the E_F, it should be shifted down to the E_F for the transport measurement or applications, which can be achieved by adding two additional electrons per unit cell to the γ-$TeSe_2$ monolayer. Figure 8(a) shows the energy bands of the -4% strained γ-$TeSe_2$ monolayer with two electrons added per unit cell. The electron doping concentration is about 1.5×10^{15} cm^{-2}, which can be experimentally realized via the current gating technologies.[51] In Fig. 8(a), the E_F now lies exactly within the band gap. The topological behavior of the band gap can be explored based on Fig. 8(a). Before calculating the topological invariants of the γ-$TeSe_2$ monolayer, the energy bands obtained from the DFT are fit with the Wannier function interpolation method. The results are shown in Fig. 8(b), indicating high consistency between the two methods. The Z_2 topological invariant is then obtained by calculating the evolution of the Wannier function center,[52] and the result is given in Fig. 8(c). The number of intersections between any horizontal reference line and the Wannier function center evolution line in half of the Brillouin zone is odd. Thus, the energy band gap concerned has $Z_2 = 1$ and a QSH insulator is obtained for the γ-$TeSe_2$ monolayer. The edge states are also investigated for the system. Figure 8(d) displays the energy bands of a semi-infinite γ-$TeSe_2$ monolayer. In the characteristic energy gap, besides a series of trivial edge states caused by the dangling bonds of the open boundary, a pair of edge states (marked by two small black arrows) appears, which connects the bottom of the conduction band and the top of the valence band. They are, thus, protected by the bulk topology. The appearance of the edge states as well as the obtained $Z_2 = 1$ in the monolayer shows that the global energy gap obtained in the γ-$TeSe_2$ monolayer is topologically nontrivial. The system remains a topologically nontrivial semimetal if tensile strain is applied as indicated in Fig. 5(f).

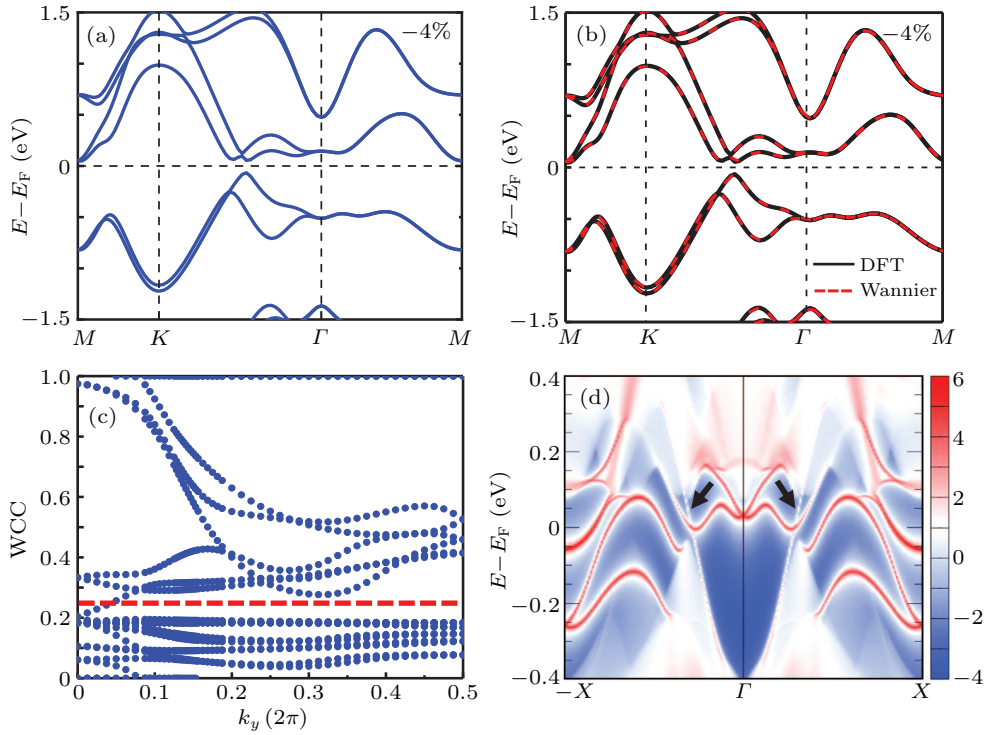


Fig. 8. (a) Energy bands of the -4% strained γ-$TeSe_2$ monolayer after doping two electrons into the unit cell. The E_F is now within the global topologically nontrivial band gap. (b) Comparison of the energy bands obtained by using the Wannier function interpolation method and the DFT. (c) The Wannier charge center evolution diagram of the material. (d) The energy bands of a semi-infinite monolayer γ-$TeSe_2$ with -4% strain. The topologically nontrivial edge states of the material are marked by arrows.

4. Conclusions

Based on the density functional theory and Wannier function method, we studied the electronic states and topological properties of the $TeSe_2$ monolayer. Numerical results show that the stable α-$TeSe_2$, β-$TeSe_2$, and γ-$TeSe_2$ are semiconductor materials with indirect gaps. The α-$TeSe_2$ is the most stable and a double degeneracy phenomenon is found in the bands of α-$TeSe_2$ and β-$TeSe_2$. When the compressive strain increases from 0% to 6%, the global topologically nontrivial band gap of γ-$TeSe_2$ is opened and increases first and then decreases. The trend is comprehended based on a competition mechanism. When the compressive strain of 3.5% is applied, the γ-$TeSe_2$ monolayer has the maximum global topologically nontrivial band gap of 0.14 eV. The topologically nontrivial feature of the material is characterized by the calculated Z_2 topological invariant and the edge state. The γ-$TeSe_2$ remains a topological semimetal with tensile strain up to 4%. Our work shows that group-VI binary 2D compounds can be new type

topological materials and have potential applications in the future electronics and spintronics.

Acknowledgement

The calculations were performed at the High Performance Computational Center (HPCC) of the Department of Physics at Fudan University.

References

[1] Novoselov K S, Geim A K, Morozov S V, Jiang D, Zhang Y, Dubonos S V, Grigorieva I V and Firsov A A 2004 *Science* **306** 666
[2] Kane C L and Mele E J 2005 *Phys. Rev. Lett.* **95** 226801
[3] Qiao Z H, Yang S Y, Feng W X, Tse W K, Ding J, Yao Y G, Wang J and Niu Q 2010 *Phys. Rev. B* **82** 161414(R)
[4] Xiao D, Yao W and Niu Q 2007 *Phys. Rev. Lett.* **99** 236809
[5] Wang Q H, Kalantar-Zadeh K, Kis A, Coleman J N and Strano M S 2012 *Nat. Nanotechnol.* **7** 699
[6] Wang H, Xu M and Zheng R K 2020 *Acta Phys. Sin.* **69** 017301 (in Chinese)
[7] Hou Y H, Zhang T, Sun J T, Liu L W, Yao Y G and Wang Y L 2020 *Chin. Phys. B* **29** 097304
[8] Geim A K and Novoselov K S 2007 *Nat. Mater.* **6** 183
[9] Novoselov K S, Fal'ko V I, Colombo L, Gellert P R, Schwab M G and Kim K 2012 *Nature* **490** 192
[10] Fang W Y, Kang W B, Zhao J and Zhang P C 2020 *Chin. Phys. B* **29** 096301
[11] Feng B J, Zhang J, Zhong Q, Li W B, Li S, Li H, Cheng P, Meng S, Chen L and Wu K H 2016 *Nat. Chem.* **8** 563
[12] Mannix A J, Zhou X F, Kiraly B, Wood J D, Alducin Diego, Myers B D, Liu X L, Fisher B L, Santiago U, Guest J R, Yacaman M J, Ponce A, Oganov A R, Hersam M C and Guisinger N P 2015 *Science* **350** 1513
[13] Guzmán-Verr G G and Lew Yan Voon L C 2007 *Phys. Rev. B* **76** 075131
[14] Chen L, Liu C C, Feng B J, He X Y, Cheng P, Ding Z J, Meng S, Yao Y G and Wu K H 2012 *Phys. Rev. Lett.* **109** 056804
[15] Vogt P, Padova P D, Quaresima C, Avila J, Frantzeskakis E, Asensio M C, Resta A, Ealet B and Lay G L 2012 *Phys. Rev. Lett.* **108** 155501
[16] Zhu F F, Chen W J, Xu Y, Gao C L, Guan D D, Liu C H, Qian D, Zhang S C and Jia J F 2015 *Nat Mat.* **14** 1020
[17] Li L K, Yu Y J, Ye G J, Ge Q Q, Ou X D, Wu H, Feng D L, Chen X H and Zhang Y B 2014 *Nat. Nanotechnol.* **9** 372
[18] Liu H, Neal A T, Zhu Z, Luo Z, Xu X F, Tománek D and Ye P D 2014 *ACS Nano* **8** 4033
[19] Cheng F and He B 2016 *Chin. Phys. Lett.* **33** 057301
[20] Zhang S L, Yan Z, Li Y F, Chen Z F and Zeng H B 2015 *Angew. Chem. Int. Ed.* **54** 3112
[21] Ji J P, Song X F, Liu J Z, Yan Z, Huo C X, Zhang S L, Su M, Liao L, Wang W H, Ni Z H, Hao Y F and Zeng H B 2016 *Nat. Commun.* **7** 13352
[22] Reis F, Li G, Dudy L, Bauernfeind M, Glass S, Hanke W, Thomale R, Schäfer J and Claessen R 2017 *Science* **357** 287
[23] Radisavljevic B, Radenovic A, Brivio J, Giacometti V and Kis A 2011 *Nat. Nanotech.* **6** 147
[24] Xu X D, Yao W, Xiao D and Heinz T F 2014 *Nat. Phys.* **10** 343
[25] Cheiwchanchamnangij T and Lambrecht W R L 2012 *Phys. Rev. B* **85** 205302
[26] Splendiani A, Sun L, Zhang Y B, Li T S, Kim J, Chim C Y, Galli G and Wang F 2010 *Nano Lett.* **10** 1271
[27] McGuire M A, Dixit H, Cooper V R and Sales B C 2015 *Chem. Mater.* **27** 612
[28] Haldane F D M 1988 *Phys. Rev. Lett.* **61** 2015
[29] Zhang J Y, Zhao B, Zhou T, Xue Y, Ma C L and Yang Z Q 2018 *Phys. Rev. B* **97** 085401
[30] Bernevig B A, Hughes T L and Zhang S C 2006 *Science* **314** 1757
[31] Chang C Z, Zhang J S, Feng X, Shen J, Zhang Z C, Guo M H, Li K, Ou Y B, Wei P, Wang L L, Ji Z Q, Feng Y, Ji S H, Chen X, Jia J F, Dai X, Fang Z, Zhang S C, He K, Wang Y Y, Lu L, Ma X C, Xue Q K 2013 *Science* **340** 167
[32] Zhu Z L, Cai X L, Yi S, Chen J L, Dai Y W, Niu C Y, Guo Z X, Xie M H, Liu F, Cho J H, Jia Y and Zhang Z Y 2017 *Phys. Rev. Lett.* **119** 106101
[33] Yan C L, Wang C, Zhou L W, Guo P J, Liu K, Lu Z Y, Cheng Z H, Chai Y, Pan A L and Ji W 2020 *Chin. Phys. B* **29** 097103
[34] Qian X F, Liu J W, Fu L and Li J 2014 *Science* **346** 1344
[35] Kresse G and Furthmuller J 1996 *Phys. Rev. B* **54** 11169
[36] Blöchl P E 1994 *Phys. Rev. B* **50** 17953
[37] Kresse G and Joubert D 1999 *Phys. Rev. B* **59** 1758
[38] Perdew J P, Burke K and Ernzerhof M 1996 *Phys. Rev. Lett.* **77** 3865
[39] Mostofi A A, Yates J R, Lee Y S, Souza I, Vanderbilt D and Marzari N 2008 *Comput. Phys. Commun.* **178** 685
[40] Wu Q S, Zhang S N, Song H F, Troyer M and Soluyanov A A 2018 *Comput Phys Commun.* **224** 405
[41] Wu B Z, Yin J R, Ding Y H and Zhang P 2017 *Sci. China Mater.* **60** 747
[42] Liu C C, Guan S, Song Z G, Yang S Y A, Yang J B and Yao Y G 2014 *Phys. Rev. B* **90** 085431
[43] Zhou T, Zhang J Y, Xue Y, Zhao B, Zhang H S, Jiang H and Yang Z Q 2016 *Phys. Rev. B* **94** 235449
[44] Liang Q F, Yu R, Zhou J and Hu X 2016 *Phys. Rev. B* **93** 035135
[45] Xue Y, Zhang J Y, Zhao B, Wei X Y and Yang Z Q 2018 *Nanoscale* **10** 8569
[46] Xue Y, Zhao B, Zhu Y, Zhou T, Zhang J Y, Li N B, Jiang H and Yang Z Q 2018 *NPG Asia Mater.* **10** 467
[47] Amorim B, Cortijo A, Juan F, Grushin A G, Guinea F, Gutiérrez-Rubio A, Ochoa H, Parente V, Roldán R, San-Jose P, Schiefele J, Sturla M and Vozmediano M A H 2016 *Phys. Rep.* **617** 1
[48] Bousige C, Balima F, Machon D, Pinheiro G S, Torres-Dias A, Nicolle J, Kalita D, Bendiab N, Marty L, Bouchiat V, Montagnac G, Souza Filho A G, Poncharal P and San-Miguel A 2017 *Nano Lett.* **17** 21
[49] Choi S M, Jhi S H and Son Y W 2010 *Phys. Rev. B* **81** 081407(R)
[50] Ren Y and Cheng F 2017 *Chin. Phys. Lett.* **34** 027302
[51] Xi X X, Berger H, Forró L, Shan J and Mak K F 2016 *Phys. Rev. Lett.* **117** 106801
[52] Yu R, Qi X L, Bernevig A, Fang Z and Dai X 2011 *Phys. Rev. B* **84** 075119